Aging and freezing of active nematic dynamics of cancer-associated fibroblasts by fibronectin matrix remodeling

Cécile Jacques[1], Joseph Ackermann[2,3†,] Samuel Bell[2†], Clément Hallopeau[1], Carlos Perez-Gonzalez[1], Lakshmi Balasubramaniam[4,11], Xavier Trepat[5,6,7,8], Benoît Ladoux[4], Ananyo Maitra[2,9], Raphael Voituriez[2,*], Danijela Matic Vignjevic[1,10,*]

[1] Institut Curie, PSL Research University, CNRS UMR 144; F-75005 Paris, France
[2] Sorbonne Université and CNRS, Laboratoire Jean Perrin, F-75005, Paris, France
[3] Laboratoire de Physique de l'Ecole normale supérieure, ENS, Université PSL, CNRS, Sorbonne Université, Université Paris Cité, F-75005 Paris, France
[4] Université Paris Cité, CNRS, Institut Jacques Monod, F-75013 Paris, France
[5] Institute for Bioengineering of Catalonia (IBEC), The Barcelona Institute for Science and Technology (BIST), 08028 Barcelona, Spain
[6] Facutltat de Medicina, Universitat de Barcelona; 08036 Barcelona, Spain
[7] Institució Catalana de Recerca i Estudis Avançats (ICREA); Barcelona, Spain.
[8] Centro de Investigación Biomédica en Red en Bioingeniería, Biomateriales y Nanomedicina (CIBER-BBN); 08028 Barcelona, Spain
[9] Laboratoire de Physique Théorique et Modélisation, CNRS UMR 8089, CY Cergy Paris Université, F-95032 Cergy-Pontoise Cedex, France
[10] INSERM, France
[11] present address: Wellcome Trust / CRUK Gurdon Institute, University of Cambridge, Cambridge, UK

† These authors contributed equally to this work

*Corresponding authors.

Email: danijela.vignjevic@curie.fr, Email: raphael.voituriez@sorbonne-universite.fr

Abstract

In the initial cancer stages, cancer-associated fibroblasts (CAFs) create a capsule around tumors. Exhibiting an elongated morphology, CAFs align with each other, closely resembling nematic ordering in liquid crystal physics. While these aligned CAFs may act as a defensive barrier hindering tumor expansion, inherent topological defects could represent weak spots, facilitating cancer cell dissemination. CAFs play a pivotal role in the genesis and remodeling of the extracellular matrix (ECM), with ECM proteins, especially fibronectin, reciprocally modulating CAF alignment and coherence. Yet, the intricate feedback loops between fibronectin deposition and CAF structuring remain largely unexplored. Here, we combined CAF live imaging, traction force microscopy, ECM microfabrication, and theoretical modeling to assess how the ECM influences the dynamics of nematically ordered CAFs. We found that CAFs dynamically orchestrate a fibronectin network that mirrors their nematic ordering. Over time, this passive nematic ordering of fibronectin, in turn, steers CAF rearrangement. Contrary to most cellular systems where defects remain dynamic at a steady state, our data highlights that the ECM/CAF interplay profoundly alters the behavior of both CAF and ECM nematics, leading to aging - massive slow down and even freezing of defect dynamics. This leads to a scenario where aligned areas and defects in CAFs layer are spatially and temporally fixed, yet active – exerting forces at the substate and transmitting forces between cells. Such a state could introduce localized vulnerabilities in the CAF layer, potentially promoting cancer cell spreading.

Introduction

The most abundant cell type in the tumor stroma is cancer-associated fibroblasts (CAFs) [1,2]. In the early stages of cancer, CAFs and the extracellular matrix (ECM) form a protective capsule that envelops tumors [3], and plays a key role in regulating their evolution. Contrary to the belief that this capsule acts passively to prevent tumor growth[4-6], we have recently found that CAFs exert active compression on cancer cells, thereby triggering mechanical signaling that slows down their proliferation [3].

The ECM is mainly produced and remodeled by CAFs [7,8]. In return, ECM proteins, in particular fibronectin, facilitate communication among fibroblasts [9-11]. This intercellular communication favors alignment within the fibroblasts, and coordinates CAFs' supracellular contractility and dynamics [3]. This results in a reciprocal relationship between ECM-induced cell activities and cell-driven ECM alterations [10,12], that were also reported for other cell types at the single cell level [13-15]; yet the impact of this interaction on the integrated organization of the ECM/CAF capsule and tumor progression is still to be understood.

CAFs have an elongated shape and tend to align with each other in a process termed "cell collision guidance" [16]. In liquid crystal physics, the alignment of the long axis of generic apolar elongated particles is described as nematic ordering[17-19]. Nematic order inherently involves "topological defects" (induced by geometric frustration, thermal fluctuations or activity), which are singular points in space where particles with different orientations meet leading to an ill-defined local alignment [17,19]. In cellular monolayers, defects have been described as spots where biologically important cellular behaviors such as extrusion, multilayering and/or polarity changes are favored [20-23]. Therefore, while the aligned CAFs within the capsule create a barrier that prevents tumor growth and spread, defects in the alignment could provide weak points, allowing cancer cells to escape. In this context, how the ECM/CAF interaction controls the nematic organization and defect dynamics of CAF monolayers and what consequences these dynamics can have on biological functions such as cancer cell dissemination remains unknown.

In this study, we combined CAFs live imaging over a long period with traction and stress force microscopy, ECM patterning, and theoretical modeling to assess how the ECM influences the dynamics of CAFs' nematic alignment. We found that CAFs dynamically orchestrate a fibronectin network that mirrors their nematic ordering. In response and over time, the passive nematic ordering of fibronectin guides the organization of CAFs. In contrast to most cellular systems described so far, and more generally of active nematic systems, in which defects have a finite density and remain dynamic even in steady state - they move, emerge, and annihilate over time [17-19,21] - we show that the ECM/CAF feedback interaction dramatically impacts the dynamics of both the CAFs and ECM nematic fields, leading to aging, massive slow down and even freezing of defect dynamics. As a result, both the aligned areas and topological defects within CAFs and ECM became stationary in both space and time but remained active, with in particular larger traction forces focused at defects, thereby opening the way to localized weakening of the CAF layer that could favor cancer cell dissemination.

Results

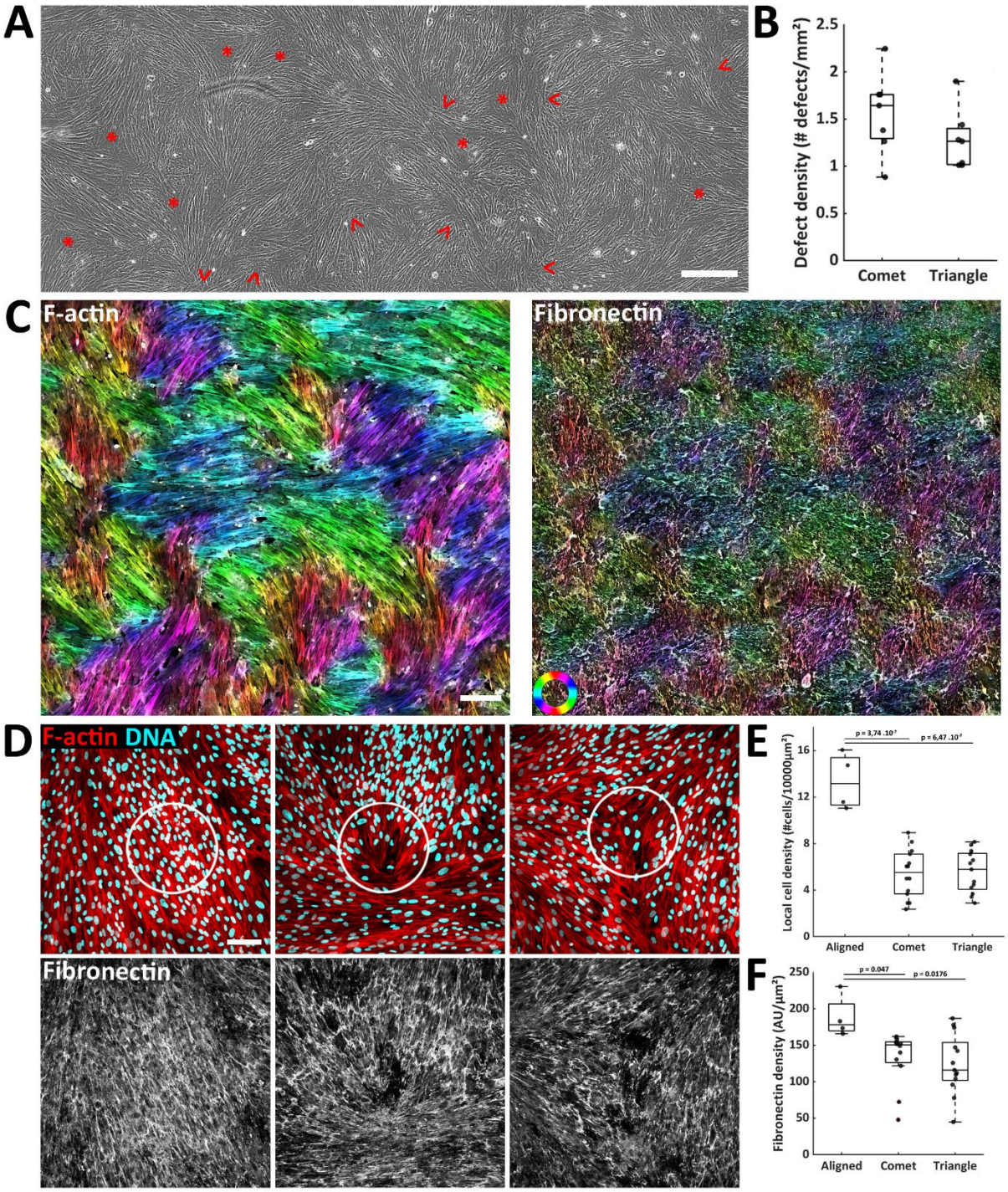

Figure 1. CAFs and fibronectin form highly correlated nematic ordered layers

A) Bright field of CAF layer cultured on an 11kPa PAA gel for 4 days. Nematic order is perturbed by topological defects: +1/2 defects or comets (arrowheads pointing towards comets' head) and -1/2 defects or triangles (stars). Scale bar: 400 µm.

B) Defect density in the nematically ordered CAF layer. Each dot represents one field of view from N=3 independent experiments. Comet, +1/2 defect, triangle, -1/2 defect. Boxplot: middle bar= median, edges bars= 25th and 75th percentiles, whiskers= extent of data.

C) Left: Orientation of CAFs based on F-actin staining (phalloidin). Right: orientation of fibronectin network stained with fibronectin antibodies. Cells or fibers with the same orientation are represented with the same color. Colored circle: orientation colormap. Scale bar: 200 µm.

D) Cell and fibronectin density in the aligned area (left), comet defect (middle), and triangle defect (right) in the CAFs layer. F-actin (phalloidin, red) and DNA (DAPI, cyan), Fibronectin (white). White circles represent the analyzed areas for each type of topology. Scale bar: 100 µm.
E) Quantification of local cell density in the aligned area, comet, and triangle defects. Each dot represents one defect, data from N=3 independent experiments. Oneway ANOVA: p-values mentioned on the graph. Boxplot: middle bar= median, edges bars= 25th and 75th percentiles, whiskers= extent of data.
F) Quantification of fibronectin density in the aligned area, comet, and triangle defects. Each dot represents one defect from N=3 independent experiments. Oneway ANOVA: p-values mentioned on the graph. Boxplot: middle bar= median, edges bars= 25th and 75th percentiles, whiskers= extent of data.

CAFs, in conjunction with the fibronectin matrix they produce, establish layers that exhibit congruent nematic ordering

To investigate whether CAFs exhibit nematic ordering similar to other elongated cells, such as myoblasts[24-26], we seeded CAFs isolated from human colorectal tumors on 11 kPa polyacrylamide (PAA) gels coated with monomeric collagen I to maintain physiological substrate rigidity[27]. Over time, CAFs established a monolayer, comprising large regions of aligned cells forming nematic order (**Fig. 1A**). This nematic ordering was disturbed locally by topological defects, with expected charges of +1/2 and -1/2, and characteristic shapes of comets or triangles, respectively. Both defect charges were observed with a similar density of 1.5 defects/mm² within the CAF layer (**Fig. 1B**).

To examine how these defects influence the deposition and organization of fibronectin by CAFs, we assessed a correlation between the orientation of CAFs (based on F-actin staining) and fibronectin once cell monolayer was confluent and nematic order fully established, approximately 6 days after cell seeding (**Fig. 1C**). The comparative analysis of orientation maps revealed a similar local orientation between CAFs and fibronectin layers, with a 92± 5% local correlation of fibers' orientation (N=4 independent experiments).

Because nematic ordering affects the local cell density (especially at defects) [15,19] and is thus expected to affect fibronectin deposition, we quantified the local density of cells and the amount of fibronectin at defects compared to aligned areas (**Fig. 1D**). We found that both types of defects contained about 2.5 times fewer cells and significantly less fibronectin compared to nearby aligned areas (**Fig. 1D-F**).

Altogether, this data shows that the deposited fibronectin fibers almost perfectly reproduce the nematic ordering of the CAFs layer.

Freezing of the CAFs active nematic is achieved after transient, aging dynamics

Typically, active nematics in both biological materials such as cell monolayers and artificial or in silico systems, can reach a chaotic stationary state in which defects emerge, move and annihilate randomly[17-19]. If the orientation of fibronectin deposition matches the local CAFs orientation consistently across space and time, then over several days, with CAFs changing dynamically, the cumulative effect of these random orientation signals should produce a

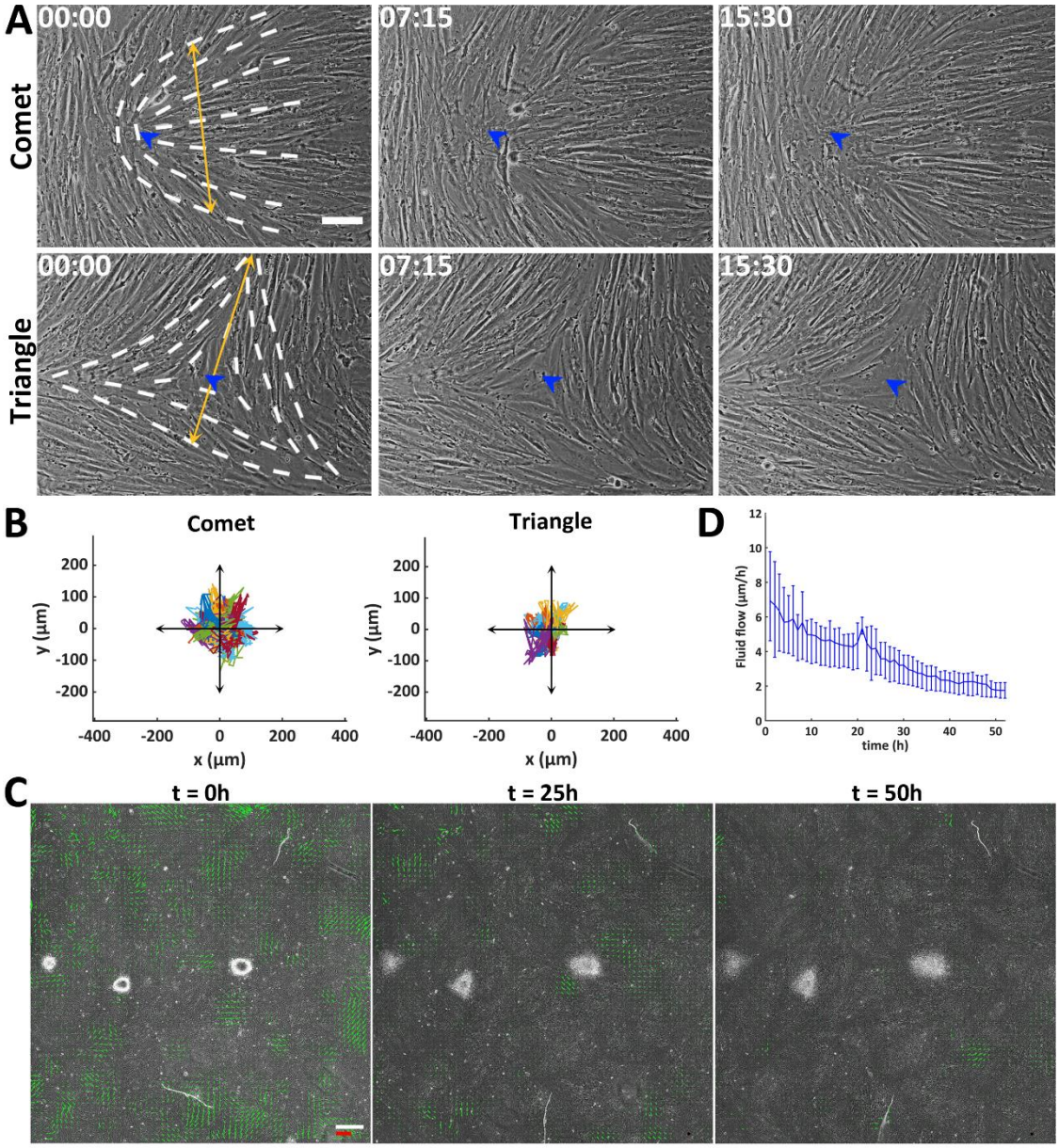

Figure 2. Defects in the CAF layer are stationary

A) Time-lapse imaging of comet (top) and triangle (bottom) defect dynamics on a bright field. Time, hours:minutes. Scale bar: 100 µm. White dashed lines highlight the shapes of defects. Yellow doubled-head arrows show where measurements for the defects' size are taken. Blue arrowheads follow the positions of defects' cores over time.

B) Trajectories of the defects' cores over time. Horizontal and vertical black doubled-head arrows represent defect size (400 µm). Each trajectory represents one defect. comet: n=50, triangle: n=39 from N=4 independent experiments.

C) Bright-field time-lapse imaging of the evolution of the velocity field of CAFs' layer over time. Green arrows represent the local velocity vectors. Red scale bar: 50 µm/h. White scale bar: 500 µm.

D) Evolution of the fluid flow (mean of the velocity field) of CAFs' layer over time. N=3 independent experiments. Error bars represent the minimum and maximum values of each time point.

fibronectin layer with uniform density and isotropic-oriented fibers. Because our observations contradicted this prediction, we questioned whether the anticipated chaotic stationary dynamics was occurring within the CAFs' layer. To investigate the dynamics of the defects, we carried out time-lapse imaging of the CAFs' layer starting 3 days after cell seeding. Over a period of 15 hours, we observed no changes in either the position or shape of the defects (**Fig. 2A**).

Quantitatively, through automatic tracking of the defects' core positions, we generated trajectories relative to the size of the defect, which provides an estimate of the error in determining the position of the defects. We found that the defect's total displacement was always significantly smaller than the typical defect's size, and thus within measurement noise (**Fig. 2B**); this indicates that no significant motion of defects, beyond fluctuations, could be observed.

This arrested dynamic is in striking contrast with the dynamic defects observed in various active nematic systems, including cell monolayers[20-22]. A natural question arises regarding the timeline of this process. To analyze the transient dynamics leading to the freezing of the CAF monolayer, we performed time-lapse imaging of the entire CAF layer starting one day after seeding (**Fig. 2C**). The quantification of the evolution of the cellular flows by PIV over time showed a global slowdown, which led to an almost complete arrest after 3 days (**Fig. 2D**).

Taken together, these results show that the dynamics of defects within the CAFs layer exhibit slowdown, or aging, which eventually leads to an arrested state.

In the nematic-ordered layer, a majority of CAFs remain stationary yet actively exert and transmit forces

We next wondered whether the stasis we observed was limited to defects or if it also applies to the individual CAFs within the nematic ordered layer. In other words, was the whole system frozen? To monitor the movement of individual CAFs, we genetically modified the CAFs to express a fluorescent marker (LifeAct-GFP), mixed 20% of these CAFs with unlabeled CAFs and started time-lapse imaging after nematic order was established. Automated tracking of the labeled CAFs over a 15-hour period revealed two distinct types of movements within the monolayer (**Fig. 3A**). While a few CAFs showed directed, linear movement with higher velocities of around 6 µm/h and persistence above 1 (see M&M for definition), the majority of CAFs (92% of n=200) appeared to be fluctuating around their initial positions, with no preferred direction of motion. These fluctuating cells displayed slower typical speeds of approximately 1 µm/h, and a persistence below 1, consistent with random motion (**Fig. 3B**). While a small subset of CAFs exhibited directed migration, most cells were only fluctuating and remained on average immobile, consistent with global freezing of the cellular flow within the full monolayer and not only of defects.

Next, we wondered if only cell motility was decreased or if CAFs, in general, became less active. As CAFs are highly contractile cells [8,10,28] we examined if they remain contractile even in stalled defects. For this, we performed traction force and internal stress microscopy to assess the force patterns generated by the CAF layer (**Fig. 3C**). For each defect topology, multiple samples were collectively averaged, using their core and direction to align them consistently (for triangle defects, one of the three equivalent directions was used). While low traction forces and internal stress without a discernible pattern were observed in aligned areas, defects show specific force patterns similar to other cellular systems that are not stalled [17,22]. In the case of comet defects, traction forces were highest at the head of the comet core with force directions pointing towards the tail of the comet, with the head of the comet showing compression and the

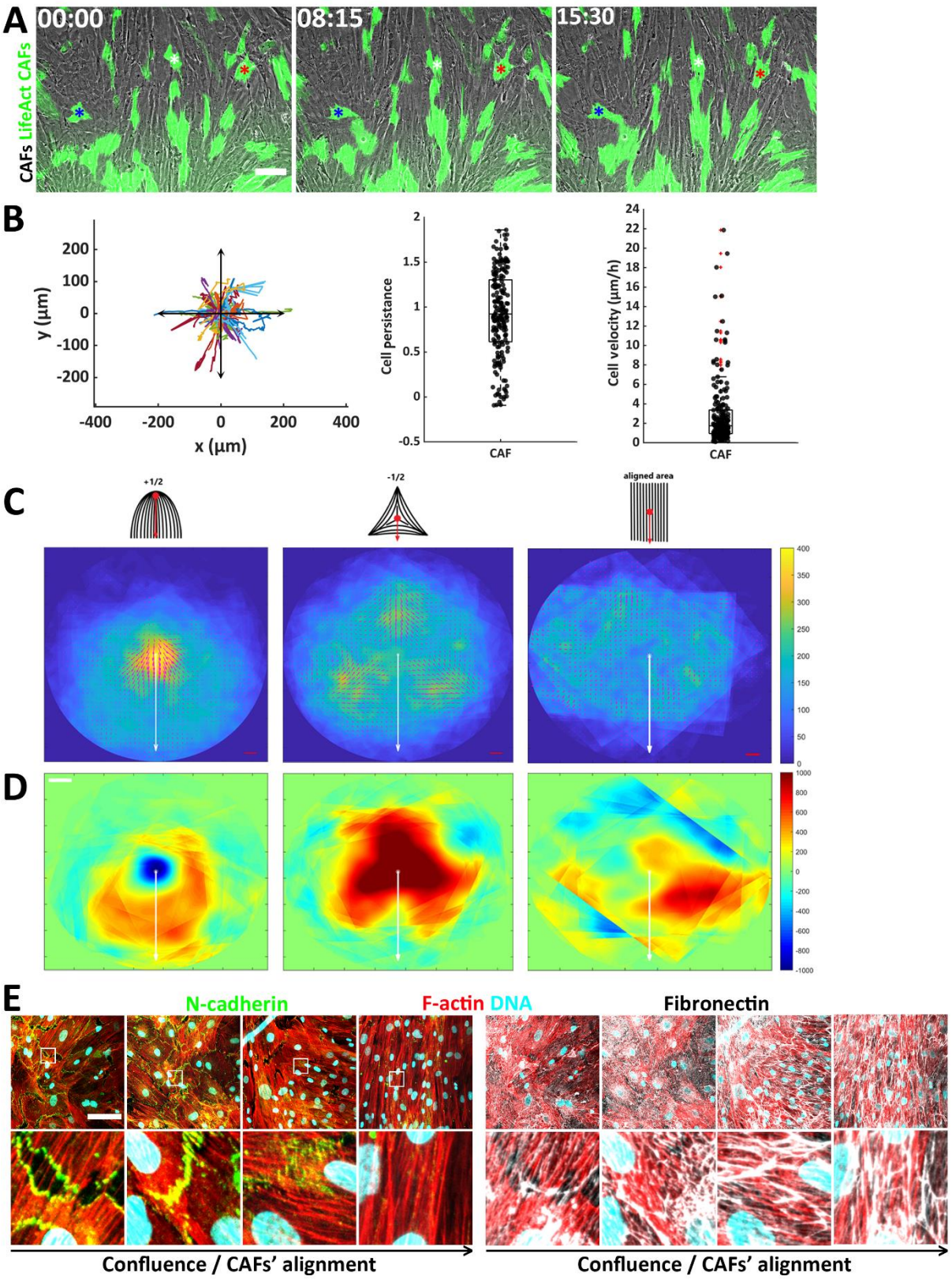

Figure 3. CAFs in the nematic ordered layer are immobile

A) Time-lapse imaging of LifeAct-GFP expressing CAFs (green) mixed with unlabeled CAFs on a bright field. Blue, white, and red stars follow the position of three different CAFs over time. Scale bar: 100 µm.

B) Left: CAFs trajectories in the whole field of view. Horizontal and vertical black double-head arrows represent defect size (400 µm). Each trajectory represents one CAF. CAFs: n=200 from N=2 independent experiments. Right: Quantification of CAFs persistence and velocity. Each dot represents one CAF. n=200 CAFs from N=2

independent experiments. Boxplot: middle bar= median, edges bars= 25th and 75th percentiles, whiskers= extent of data, red cross= outliers.
C) Schemes representing the core and the direction used to average aligned areas, comet, and triangle defects. Average of traction force magnitude maps (colormap) and vectors (pink arrow) for aligned areas, comets, and triangle defects. White stars and vectors correspond to the red dot and vectors of the respective scheme. Red scale bar: 400 Pa. n=50 comets, n=42 triangles, n=18 aligned areas from N = 4 independent experiments.
D) Average of internal stress maps for aligned areas, comets, and triangle defects. White stars and vectors correspond to the red dot and vectors of the respective scheme in (C). White scale bar: 100 µm. N = 4 independent experiments, comets n=50, triangles n=42, aligned areas n=18.
F) CAF layer at different confluence and alignments stained for F-actin (phalloidin, red), DNA (DAPI, cyan), N-cadherin (green), and fibronectin (white). White boxes represent the positions of the magnified regions. Scale bar: 100 µm.

tail displaying tension (**Fig. C, D,** left panels). For triangle defects, peaks of traction forces were evident at each triangle vertex with forces directed towards the triangle core; with the center of the triangle under tension (**Fig. C, D,** middle panels). Thus, even though CAFs and defects in their nematic layer are frozen, they are still active as cells continue to exert forces.

Such distinctive patterns at defects could potentially stem from the supracellular units formed between CAFs. Indeed, the low traction forces observed in the aligned area suggest that forces are transmitted between the CAFs. As comet core and triangle vertices are the termini of aligned areas, the transmission of forces between CAFs is abolished and forces are transmitted to the substrate, resulting in the visible peaks of traction in both cases.

A possible candidate for such interconnections between CAFs is N-cadherin, a key cell-cell adhesion protein in mesenchymal cells[29]. Alternatively, CAFs could be linked via stitch adhesions with fibronectin acting as a glue[9,11]. To examine how CAFs were connected, we stained for N-cadherin and fibronectin in CAF layers of varying densities (**Fig. 3E**). At lower densities, where CAFs were more spread out and less aligned, we observed N-cadherin at cell-cell junctions. However, as cell density increased, leading to elongated, nematic-ordered CAFs, N-cadherin presence diminished. Conversely, fibronectin puncta, which were already present at lower cell densities, increased in amount as the CAF density increased. These findings suggest that in a nematic ordered layer, CAFs may be indirectly interacting via fibronectin.

Therefore, the observed lack of directed movement of both defects and individual CAFs within nematic layers could be attributable to fibronectin depositions interposed between CAFs and the substrate, potentially immobilizing the system.

Fibronectin depletion restores the dynamics of cells and defects in CAF nematic layer

To assess whether the immobilization of the CAFs layer dynamics was indeed a result of fibronectin deposition, we depleted fibronectin in CAFs using siRNA (**Fig. 4A**) and performed time-lapse imaging (**Fig. 4B**). By tracking individual cells using Hoechst labeling of nuclei, we observed that fibronectin-depleted cells (siFN) exhibited longer and straighter trajectories (**Fig. 4C**), and moved with greater persistence and speeds (**Fig. 4D**), compared to CAFs treated with control siRNA (siCtrl). Thus, upon depletion of fibronectin, the mobility of CAFs within the layer significantly increased.

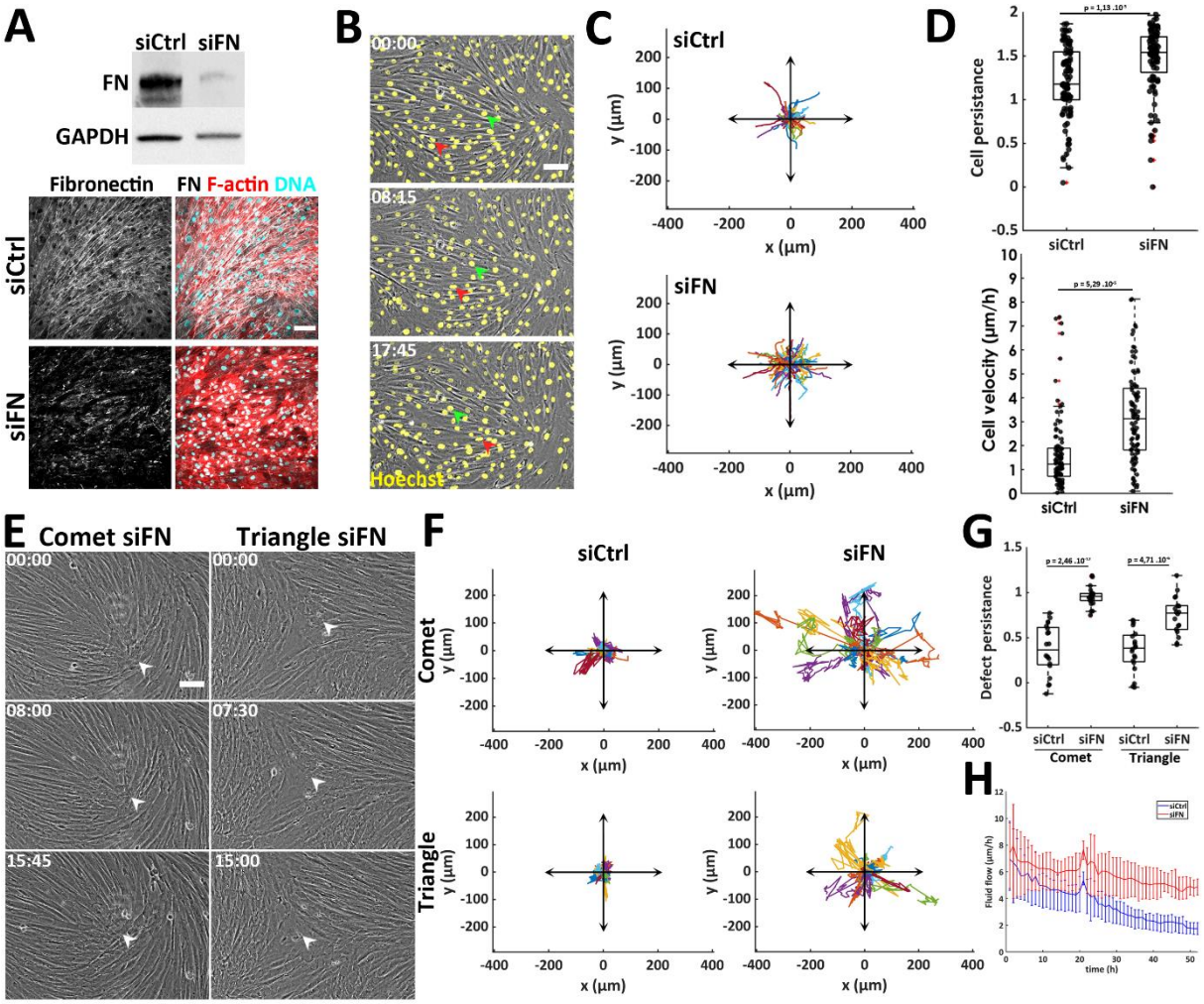

Figure 4. Dynamics of defects and CAFs is restored upon fibronectin depletion

A) Depletion of fibronectin in CAFs evaluated by western blot (top) and immunofluorescence (bottom). Cells were transfected with either control siRNA (siCtrl) or siRNA against fibronectin (siFN). GAPDH was used as a loading control. Cells stained for F-actin (phalloidin, red), DNA (DAPI, cyan), and fibronectin (white). Scale bar: 100 µm.

B) Bright field time-lapse imaging of CAFs transfected with siRNA against fibronectin (siFN) and labeled with Hoechst (yellow). Each arrow (red and green) follows one CAF trajectory over time. Time, hours:minutes. Scale bar: 100 µm.

C) Trajectories of CAFs transfected with either control siRNA (siCtrl) or siRNA against fibronectin (siFN). Horizontal and vertical black double-head arrows represent defect size (400 µm). Each trajectory represents one CAF. n=100 CAFs from N=2 independent experiments.

D) Quantification of persistence and velocity of CAFs transfected with either control siRNA (siCtrl) or siRNA against fibronectin (siFN). Each dot represents one CAF. n=100 CAFs for each condition from N=2 independent experiments. Velocity, t-test: p-values mentioned on the graph. Persistence, t-test: p-values mentioned on the graph. Boxplot: middle bar= median, edges bars= 25th and 75th percentiles, whiskers= extent of data, red cross= outliers.

E) Bright field time-lapse imaging of defect dynamics in fibronectin depleted CAFs layers (siFN). White arrows follow the defect core trajectory over time. Time, hours:minutes. Scale bar: 100 µm.

F) Trajectories of defect cores in control (siCtrl) and fibronectin-depleted (siFN) CAFs layers. Horizontal and vertical black double-head arrows represent defect size (400 µm). Each trajectory represents one defect. siCtrl: comet n=20, triangle n=20; siFN: comet n=24, triangle n=18. N=5 independent experiments.

G) Quantification of the persistence of defects in control (siCtrl) and fibronectin-depleted (siFN) CAFs layers. Each dot represents one defect. N=5 independent experiments, siCtrl: comet n=20, triangle n=20; siFN: comet n=24, triangle n=18. Persistence, t-test: p-values mentioned on the graph.

H) Evolution of the fluid flow (mean of the velocity field) of control (siCtrl, blue) and fibronectin-depleted (siFN, red) CAFs' layer over time. N=3 independent experiments. Error bars represent the minimum and maximum values of each time point.

Subsequently, we assessed whether the increased motility of CAFs in the absence of fibronectin also influenced the dynamics of defects in the CAFs' nematic layer. To that end, we performed time-lapse imaging of CAFs treated either with siCtrl or siFN (**Fig. 4E**). Automated tracking of the cores of defects revealed that in the absence of fibronectin, defects become mobile (**Fig. 4F, G**). Indeed, while defects in the layer of control CAFs fluctuated around their initial position (**Fig. 4F**), defects in the fibronectin-depleted CAFs layer exhibited longer and straighter trajectories (**Fig. 4F**), moving with greater persistence (**Fig. 4G**). In particular, comet defects were motile, moving along their head-tail direction, indicating that fibronectin-depleted CAFs were forming a contractile nematic system[18,22]. Triangle defects, in contrast, displayed lower speeds and persistence compared to comet defects, likely due to a lack of a preferred migration direction[20], as expected in active nematics.

Finally, for fibronectin-depleted CAFs, the slowdown of cellular flows was significantly less pronounced and did not lead to freezing observed in control CAFs (**Fig. 4H**).

Therefore, the fact that both individual cells and defects remain more dynamic in the absence of fibronectin suggests that fibronectin deposition is causing the freezing or aging, of the system.

Established fibronectin patterns freeze CAF nematic dynamics and migration of individual cells

Until now, we showed that CAF nematic ordering generated fibronectin patterns with the same nematic order and that such fibronectin deposition was necessary for freezing the system. To further characterize the mechanism of freezing, we tested if the interaction of CAFs with a pre-existing fibronectin pattern could be sufficient to induce the freezing of the dynamics of the CAF layer. For this, we cultured CAFs on PAA gels, allowing them to create nematic ordering and a corresponding fibronectin layer replica (**Fig. 5A**). Subsequently, we removed the CAFs to obtain fibronectin patterns with nematic ordering (**Fig. 5B**, fibronectin 1). On those fibronectin patterns, we then seeded new CAFs. Once these CAFs formed a confluent layer, we determined the organization of CAFs by staining their F-actin (**Fig. 5B**, F-actin). The comparative analysis of orientation maps revealed a similar local orientation between fibronectin patterns and CAFs layer (**Fig. 5C**). We also stained for newly deposited fibronectin (**Fig. 5B,** fibronectin 2) and found that the organization of the newly deposited fibronectin mirrored the pre-existing fibronectin pattern (**Fig. 5C**). These data show that the fibronectin pattern was instrumental in instructing the CAFs to align into its specific nematic ordering configuration.

Next, we explored if fibronectin patterns or, alternatively, fibronectin depositions between CAFs, were responsible for freezing CAF nematics. To discriminate between these possibilities, we produced fibronectin nematic patterns as described above and seeded either control CAFs (siCtrl) or fibronectin-depleted CAFs (siFN) on top of them. As observed above, CAFs aligned according to the fibronectin nematics and defects (**Fig. 5D**). Over a 15-hour period, no differences were observed in defect position (**Fig. 5E**). Indeed, both, control and fibronectin-depleted CAFs fluctuated around their position, with a fluctuation range smaller

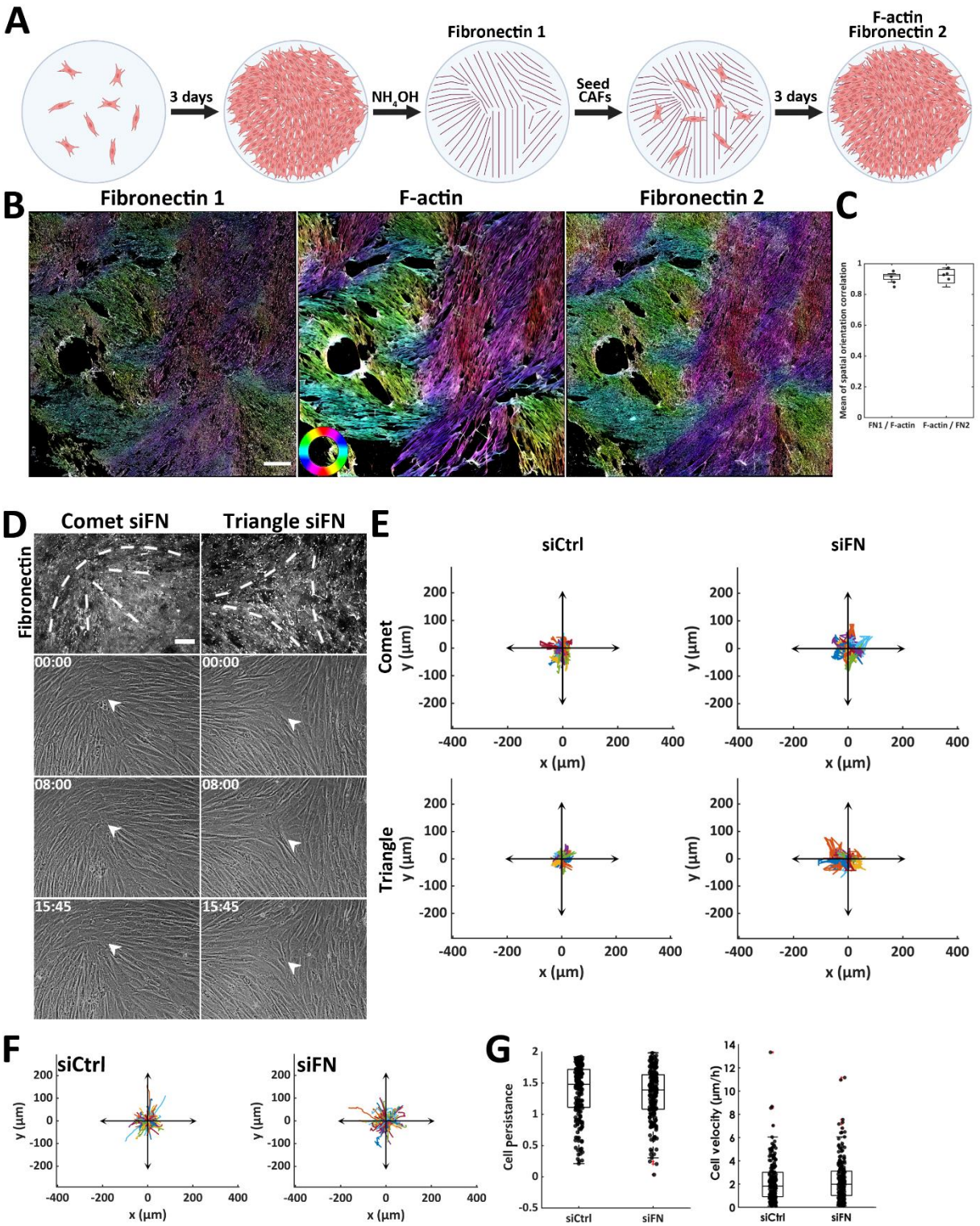

Figure 5. Fibronectin patterns freeze CAF nematics

A) Scheme representing the experiment design: CAFs were seeded on 11kPa PAA gel and cultured for three days. CAFs were removed using NH_4OH, and deposited fibronectin was stained using specific antibodies (Fibronectin 1). On those fibronectin patterns, new CAFs were seeded and cultured for an additional three days. Cells were then fixed, and stained for F-actin and fibronectin (Fibronectin 2, representing the sum of fibronectin pattern and newly deposited fibronectin).

B) The orientation map of the fibronectin pattern (Fibronectin 1), the CAFs layer seeded on it (F-actin), and the final fibronectin network (Fibronectin 2, representing the sum of fibronectin pattern and newly deposited fibronectin). Each color represents one orientation of either the fibronectin fibers or the CAFs. Colored circle: orientation colormap. Scale bar: 400 µm.

C) The mean of the local spatial orientation correlation between the CAFs (F-actin) and the fibronectin pattern (Fibronectin 1) and CAFs (F-actin) and final fibronectin deposition (Fibronectin 2). Each dot represents one pair of F-actin and fibronectin patterns from N=4 independent experiments. Boxplot: middle bar= median, edges bars= 25th and 75th percentiles, whiskers= extent of data.
D) Fibronectin stained with specific antibodies, highlights defects - comet (left) and a triangle (right). White dashed lines represent the shape of the comet (left) and triangle (right). Bright-field time-lapse imaging of defect dynamics in fibronectin-depleted CAFs layers (siFN) seeded on those preformed fibronectin patterns. White arrowheads follow the positions of defects' cores over time. Time, hours:minutes. Scale bar: 100 µm.
E) Trajectories of defect cores in control (siCtrl) and fibronectin-depleted (siFN) CAFs layers seeded on preformed fibronectin patterns. Horizontal and vertical black double-head arrows represent defect size (400 µm). Each trajectory represents one defect. siCtrl: comet n=18, triangle n=12; siFN: comet n=17, triangle n=15 from N=3 independent experiments.
F) Trajectories of control CAFs (siCtrl) and fibronectin-depleted CAFs (siFN) seeded on on preformed fibronectin patterns. Horizontal and vertical black double-head arrows represent defect size (400 µm). Each trajectory represents one CAF. n=200 for each condition from N=3 independent experiments.
G) Quantification of persistence and velocity of CAFs transfected with either control siRNA (siCtrl) or siRNA against fibronectin (siFN) and seeded on a fibronectin pattern. Each dot represents one CAF. n=200 CAFs for each condition from N=3 independent experiments. Boxplot: middle bar= median, edges bars= 25th and 75th percentiles, whiskers= extent of data, red cross= outliers.

than the defects' size (**Fig. 5E**), thus indicating that no significant motion could be observed beyond fluctuations. By tracking individual CAFs within the nematic layer, we found that fibronectin patterns were also sufficient to arrest the migration of individual cells, independently of whether they produce fibronectin (**Fig. 5F, G**).

Therefore, fibronectin patterns alone were sufficient to arrest the migration of CAFs and defects within the CAFs layer, even if CAFs are unable to produce fibronectin.

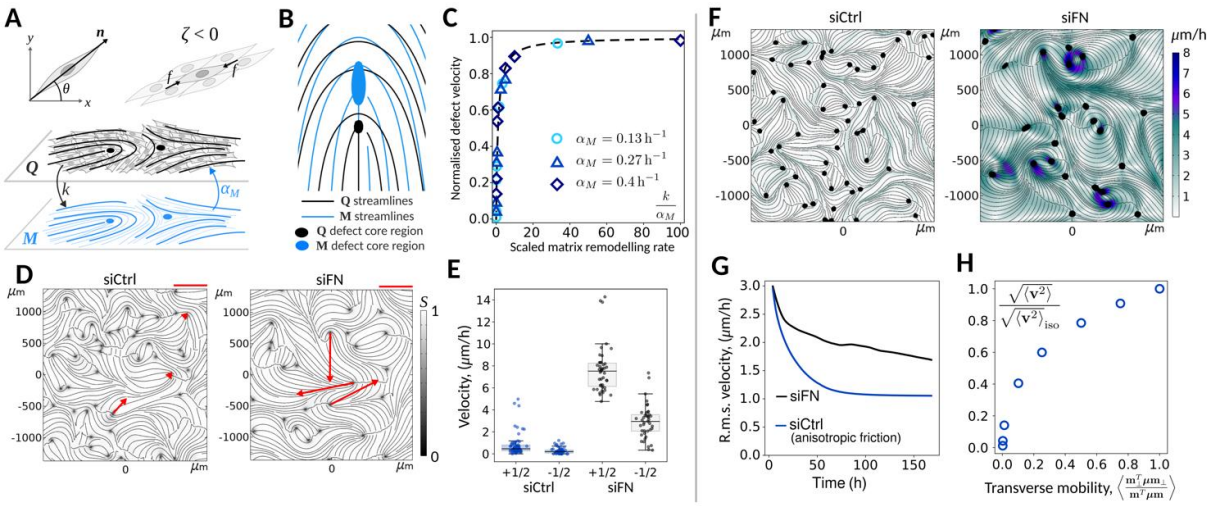

Figure 6. Theoretical model

A) The fibroblast layer is modelled as an active nematic with a vector along the major axis of the cells, **n**, being used to define the nematic order parameter **Q**. They exert an active stress -ζ**Q**, where the parameter ζ is introduced in Eq. 4; ζ < 0 for the contractile fibroblast layer. Fibroblasts deposit fibers (with nematic alignment **M**) onto a surface with rate k, and fibroblasts also reorient actively to the matrix with coupling α_M.
B) Numerical visualization of interacting fibroblast (blue) and matrix (black) +1/2 defects. The core region is shown as the region for which S < 0.42, S_M < 0.35.
C) The comoving defects' velocity as a function of the scaled remodeling rate k/α_M for different values of the matrix coupling α_M. The velocities are normalised by the numerical velocity value as $k \to +\infty$. The theoretical scaling for v/v_0 predicted in Eq. (5) is indicated by the black dashed line.

D) Fibroblast patterns with (siCtrl) and without (siFN) matrix production (**Q** streamlines in black). The shading indicates the degree of nematic order S (defect cores are shaded black). Velocities of selected +1/2 defects are indicated by red arrows. Velocity scale bar: 5 µm/h.
E) Quantification of the defect velocities for both +1/2 and -1/2 defects with (siCtrl) and without (siFN) matrix production. Each dot represents one defect. The parameters are chosen so that the velocities obtained from the numerical study correspond to the experimental velocities.
F) Flow velocity heatmaps at 72h with (siCtrl) and without (siFN) matrix production, in the case of anisotropic friction ($\mu_\perp/\mu_0$ = 0.0001). **Q** streamlines are given in black, with defect core regions indicated by black circles.
G) The evolution of the root mean square flow velocity over time with (siCtrl, blue) and without (siFN, black) matrix production, with an anisotropic friction ($\mu_\perp/\mu_0$= 0.1).
H) The root mean square flow velocity—scaled by its value with isotropic friction—as a function of the average normalized mobility perpendicular to the matrix direction (a proxy for the degree of anisotropic friction).
Parameter values, where not written explicitly in the caption, are listed in Table S1 in the Supplementary Model.

A minimal model of active nematic with coupling to a dynamic, passive nematic field recapitulates the observed aging and freezing dynamics

So far, experimental observations show that CAFs behave as an active nematic layer that produces a fibronectin matrix with coinciding nematic order and that CAFs respond and align with a pre-existing nematically order matrix; as opposed to active nematic systems described so far, which exhibit a dynamic stationary state, this coupling was found to induce aging dynamics that eventually lead to a frozen state with immobile topological defects and no observable cellular flow despite local active fluctuations. Based on active nematic hydrodynamics, we proposed a minimal 2-dimensional model of the CAF layer that recapitulates these observations and confirms that indeed the interaction with a deposited nematic matrix induces a feed-back that can lead to freezing (**Fig. 6A**). The model describes minimally the dynamics of the nematic order parameter Q of the CAF layer building up on classical active nematohydrodynamics[17,19,22,24] (see supplementary model (SM) for details):

$$\frac{DQ}{Dt} = \frac{H}{\gamma} - \lambda E + \alpha_M M \qquad (1)$$

where $D\,Q/Dt = \partial_t Q + (v.\nabla)Q - (Q.\Omega - \Omega.Q)$ is the corotational convective derivative, $H = -\delta\,F/\delta\,Q$ is the so-called molecular field, γ the rotational viscosity, $\Omega = (\nabla v - (\nabla v)^T)/2$ the vorticity, λ a flow alignment coupling, $E = (\nabla v + (\nabla v)^T)/2$ the strain rate tensor, and F the standard free energy of a nematic field that would control the dynamics in absence of activity (see SM). The key ingredient that we introduce is the nematic matrix field M that encodes the strength and direction of the fibronectin matrix alignment; in turn, the response of the CAF nematic order to the matrix is taken into account *via* a phenomenological active coupling α_M in (1), which favors the alignment of Q with M. The assembly-degradation dynamics of M can be minimally encoded as

$$\partial_t M = k(Q - M), \qquad (2)$$

where k is the turnover rate. Finally, force balance on the CAF's layer can be written

$$\xi v = -\nabla P - \zeta\nabla.Q + \eta\nabla^2 v - H.\nabla Q + \lambda\nabla.H + \nabla.(Q.H - H.Q) \qquad (4)$$

where $\xi(M)$ is a potentially anisotropic friction tensor that can depend on M, P a pressure, ζ a phenomenological coupling defining the active stress, and η the viscosity. For the sake of simplicity, we first assumed that the friction ξ is independent of M, and considered limit

regimes of either fully compressible (neglecting P in (4)) or incompressible (where P is a Lagrange multiplier enforcing $\nabla . v = 0$). Numerical analysis of the model, in agreement with analytical arguments following Ref[30], shows that the velocity of isolated +1/2, comet defects is given in steady state by

$$v = \frac{v_0}{1+\alpha_M/k}, \qquad (5)$$

where v_0 is a velocity scale independent of k (see SM), and can thus be dramatically decreased for either a slow matrix turnover rate ($k \to 0$) or strong alignment interaction α_M (**Fig. 6B-C**), which can be interpreted as the relaxation rate of the nematic field Q to the matrix field. The slow down and even arrest of defects, as is observed in experiments, can thus be triggered by the alignment interaction α_M only, even for a friction ξ assumed independent of M. The numerical analysis of the model shows that this sole process reproduces the expected difference in the defect velocities for siCtrl and siFN (**Fig. 6D-E**). Of note, in this case, cellular flows are maintained even in the limit ($k \to 0$) of arrested defects (see SM). To reproduce the observed decrease of both defects speed and cellular flow speeds in siCtrl experiments, we thus made the further hypothesis that friction is anisotropic and depends on M according to $\xi = aI + bM$ where a, b are phenomenological functions of the norm of M given in SM. This form is consistent with the observed anisotropy in single-cell dynamics (**Fig. 3B**), and indeed yields an aging dynamics of the flow field, with a significant decrease in cellular flow speeds over time (**Fig. 6F-H**). Finally, an active hydrodynamic model of the CAF layer shows that the interaction with a deposited nematic matrix induces feedback that can lead to a slowdown and eventually freezing of the dynamics of both defects and cellular flows.

Discussion

In this study, we demonstrate that fibronectin fiber-derived passive nematics hinder the dynamics of the active nematic CAFs layer. This effect results in the immobilization of both individual cells and the defects within the CAFs layers. This passive nematic formation stems from the CAFs laying down a fibronectin network that mirrors their inherent nematic order. Notably, this leads to a reduced presence of CAFs and a diminished fibronectin density at defect cores. The primary deposition of fibronectin echoes the nematic organization of the CAFs, which in turn guides the CAFs layer to maintain this specific nematic arrangement. As the CAFs persistently deposit fibronectin following this blueprint, a reinforcing feedback loop between the CAFs and the fibronectin layer emerges. This feedback culminates in a system that progressively solidifies, becoming static over time.

The fibronectin deposition does not only halt the movement of defects, but it also restricts the movement of individual CAFs within the layer. This immobilization allowed for the formation of supracellular units consisting of CAFs connected by fibronectin stitch adhesions. These units subsequently generated unique force patterns at defects. The force pattern at comet defects was similar to those observed in MDCK at comet defects where cell extrusion occurs [22]. In tumors, the topological organization of ECM and CAFs correlates with the invasive stage of the tumor and is termed tumor-associated collagen signatures (TACS) [31,32]. TACS-2 is identified in non-

invasive regions of the tumor and is characterized by CAFs and the ECM running parallel to the tumor edge[8]. On the other hand, TACS-3 is associated with invasive regions where CAFs and the ECM are organized perpendicular to the tumor edge, where they serve as highways for tumor dissemination[8]. Thus, it is possible that CAF extrusion occurs at the comet defects, which could be followed by a reorientation of these CAFs from parallel to perpendicular to the tumor periphery, and thus switch from TACS2 to TACS3.

The force pattern at triangle defects suggests that the CAF layer could potentially pinch the substrate and tumor cells below. This could result in a piercing of the CAF layer and consequently facilitate cancer invasion. Considering the lengthy nature of tumor invasion, the immobilized state of defects could inadvertently promote this invasive activity.

In the future, it would be interesting to investigate where cancer cells breach the CAF barrier during cancer invasion. If the breach occurs at defects, understanding the precise mechanisms leading to invasion at these locations could help devise strategies to combat it, potentially preventing metastasis formation in patients.

Acknowledgments: We thank all members of the DMV lab and Pascal Silberzan for helpful discussions. We acknowledge Vincent Fraisier, Chloe Guedj and Lucie Sengmanivong from the Cell and Tissue Imaging Facility (PICT-IBiSA). This work received funding from the European Union's Horizon 2020 research and innovation program: European Research Council (ERC) under the grant agreement CoG 772487 (DMV), AdvG 883739 (XT), AvdG 101019835 (BL), Aviesan ITMO Cancer « Convention Frontières du Vivant» N°18CF156-00 (CJ), Fondation pour la Recherche Médicale - FRM FDT202106013007 (CJ), Institut National du Cancer INCa 16712 (BL), the Ligue Contre le Cancer (Equipe labellisée 2019) (BL), LABEX Who Am I? (ANR-11-LABX-0071) (BL), SyG SHAPINCELLFATE (RV), Fondation ARC pour la Recherce sur le Cancer (CPG), and ANR (RV), EPSRC grant no EP/R014604/1 (AM). AM was supported in part by a TALENT fellowship awarded by CY Cergy Paris Université. AM would like to thank the Isaac Newton Institute for Mathematical Sciences, Cambridge, for support and hospitality during the program New statistical physics in living matter: non equilibrium states under adaptive control where a part of the work on this paper was undertaken.

Material and methods

Cell culture

For this study, we have used CAFs isolated from colon tumor samples of a patient treated at Institut Curie Hospital, Paris, with the patient's written consent and approval of the local ethics committee. CAFs were extracted from fresh tumor samples and immortalized as described earlier[1–3]. CAFs were cultured on 30kPa soft substrate plates (ExCellness – PrimeCoat, Biotech SA). Before being used, plates were plasma-treated for 30s at 800 mTorr and then coated with 5 µg/mL of monomeric collagen in DMEM supplemented with 2% Anti-Anti, 12.5 µg/mL Metronidazole B (Braun), and 4 µg/mL Ciprofloxacin (Panpharma). After incubation overnight at 37°C, 5% CO_2, dishes were washed with some medium before adding the CAFs medium

(DMEM 5% FBS and 1% ITS-A) and seeding approximately $1x10^6$ CAFs. CAFs were left to grow for one week at 37°C 5% CO_2 before being used for experiments.

LifeAct GFP transfection

Fibroblasts were transfected with LifeAct GFP using lentiviral infection. Lentiviruses containing the LifeAct GFP plasmid with 4 µg/mL of Polybrene were added to fibroblasts and incubated overnight at 37°C, 5% CO_2. After incubation, fibroblasts were washed several times with media and then incubated at 37°C 5% CO_2. After a few days, the transfection success was checked using a fluorescent microscope. Once the fibroblasts population reached 15 to 20 million cells, fibroblasts were sorted to remove GFP-negative fibroblasts. Sorted fibroblasts were then cultured as described above.

PAA gel preparation

PAA gels at 11 kPa were prepared on Glass-bottom dishes (Fluorodish, plate 35 mm Ø, Glass 23 mm Ø, WPI). First, plates were treated with 3-amino-propyltrimethoxysilane (diluted 1:2 with PBS; Sigma-Aldrich/Merck) for 15min at RT. After three washes with MilliQ water and an air drying, dishes were treated with glutaraldehyde 0.25% in PBS (Sigma-Aldrich/Merck) for 30 min at RT. After three washes with MilliQ water and an air drying, PAA solution for 11 kPa gels were prepared by mixing in 368.5 µL of PBS, 93.75 µL of 40% acrylamide (Bio-Rad), 25 µL of 2% bis-acrylamide (Bio-Rad), 2.5 µL of 10% ammonium peroxodisulfate (VWR) and 0.25 µL of tetramethylethylenediamine (Euromedex). For traction force microscopy experiments, 5 µL of 0.2 µm red beads FluoSpheres carboxylate-modified (580/605, Invitrogen) were added to the PAA gel solution. 25µL drops of the PAA gel solution were put in the middle of the dish and covered with 18 mm diameter glass coverslips. PAA gels were let to polymerize for one hour at RT. Once PAA was polymerized, PBS was poured into dishes, and glass coverslips were removed using a scalpel and a tweezer. PBS was removed, and 100 µL of 2 mg/mL sulfo-sanpah (Sigma-Aldrich/Merck) was added only onto PAA gels. Dishes with sulfo-sanpah were then treated with ultraviolet light (365 nm; 5cm from source) for 5 min. PAA gels were washed briefly with 10 mM HEPES, followed by two washes with PBS. Dishes were then incubated with 200 µL of 100 µg/mL monomeric collagen I (Rat tail origin, Corning) diluted in 0.2% acetic acid pipetted only on the PAA gel at 4°C overnight. Dishes were washed with PBS before the addition of CAFs and culture medium.

Time-lapse imaging of nematic ordering evolution over time

$15x\ 10^4$ CAFs, treated with either control siRNA (siCtrl) or siRNA against fibronectin (siFN), were seeded on 11 kPa PAA gel. After planting, fibroblasts were incubated in DMEM medium containing 10% FBS, 1% ITS-A, 2% Anti-Anti, 12.5 µg/mL Metronidazole (B. Braun), and 4 µg/mL Ciprofloxacin (Panpharma) at 37°C 5% CO_2 for 24h before imaging. CAFs were imaged using an inverted Eclipse Ti-2 microscope (NIKON) driven by NIS elements (Nikon) with a

fully motorized stage, a 10X (NA, 0.3) objective, and an incubation system at 37°C, 5% CO_2. The entire CAFs layers of each condition were imaged. Time-lapse imaging lasted 50 to 70h, with images taken every 1h.

2D traction force microscopy experiment

CAFs were seeded on 11 kPa PAA gel with red beads (580/605, Invitrogen, F8810) and cultured in DMEM medium containing 10% FBS, 1% ITS-A, 2% Anti-Anti, 12.5 µg/mL Metronidazole (B. Braun), and 4 µg/mL Ciprofloxacin (Panpharma) at 37°C 5% CO_2. The number of cells seeded depended on the desired cell density at the moment of imaging. During siRNA experiment, CAFs were treated with either control siRNA (siCtrl) or siRNA against fibronectin (siFN). CAFs were imaged using an inverted Eclipse Ti-E microscope (NIKON) driven by Metamorph software (v.7.8.13.0) with a fully motorized stage, a 10X (NA, 0.3) objective, and an incubation system at 37°C, 5% CO_2. Beads were imaged using 562/40 nm excitation and Bright Field was used to image the CAFs. For some experiments, 472/30 nm excitation was used to image LifeAct-GFP CAFs, while 377/50 nm excitation was used for Hoechst staining. For each region of interest focusing on one type of topology: two single z slices were taken, one focusing on the fibroblast plane and one focusing on the beads. Time-lapse imaging lasted for ~16h, with images taken every 15 min. At the end of imaging, dishes kept on the microscope stage were carefully washed with PBS before cells were removed with TrypLE Express (ThermoFisher). Once cells detached from PAA gels, one-time point acquisition was performed for all positions to obtain the reference points for relaxed gel.

2D traction analysis

Using Matlab, traction force experiments were analyzed using scripts developed by [33]. First, data were separated into folders corresponding to each position, then positions were treated separately. For each position, all images were corrected for potential drift, aligned, and cropped the same way using the image of beads after trypsin treatment as a reference. Using the Particle Image Velocity (PIV) method, the displacement of the beads between traction and trypsin images was measured on eight-by-eight pixels squares along all images with overlapping between each square to precise the measure. From the displacement and the gel settings (finite thickness), traction forces were calculated using Fourier-transform traction microscopy. The traction magnitudes' maps were plotted for each time point and traction vectors were plotted on top of the cell images.

Internal stress analysis

Internal stresses of the cell layer were analyzed using Bayesian Inversion Stress Microscopy (BISM) script developed by [34] using Matlab. Internal stresses were calculated from the traction forces obtained previously using Bayesian inversion theory. BISM doesn't depend on the physical property of the system such as tissue rheology, and thus doesn't need boundary

conditions. However, the system needs to have a small height compared to its planar surface and is not reliable very close to the boundary. BISM is based on strong statistical hypotheses such as the Gaussian distribution of the stresses. Tests performed by Vicent Nier have shown that BISM is robust and could be applied to different systems as long as they validate the height condition. Only defects inside the layer were taken to avoid boundary issues. In addition, the height condition was validated in this study as the fields of view are 825.6 µm by 598.56 µm, and CAFs height is about 10-15 µm, so BISM can be applied.

Defects averaging

Matlab was used to do the analysis. For each experiment, positions were separated into different types of topology: comet defects, triangle defects, and aligned areas. Positions of each type of topology were then aligned in the same direction. To do so, the core and direction places of the defect/aligned area were pointed out of the bright field images (see Fig3.C for a visual representation of core and direction places for each type of topology). For each position and time point, core-centered circles with a radius of 800 pixels were used as masks. These circular masks were applied to traction force, and internal stress maps to only keep data within the masks. Rotations of these circular masks with traction force and internal stresses were then performed to align their directions. Finally, for each type of topology, the averages of all the circles were done to obtain their specific force pattern organization.

Immunostaining

Immunostainings were performed using CAFs growing on 11 kPa PAA gels described above. Cells were pre-extracted before being fixed. To do so, a 50 mL 2X PEM solution was prepared in MilliQ water with 3g PiPES, 1 M $MgCl_2$, 100 mM EGTA and PH adjusted at 6.9 using KOH. First, cells were washed with PBS and then incubated for 30 s at RT with the extraction solution (0.2% Triton X-100, 50% 2X PEM, 4% PEG 35000 and 5 µM Phalloidin in PBS). Cells were washed two times with the rinse solution (50% 2X PEM, 2 µM Phalloidin in MilliQ water) and then incubated in 4% PFA in PBS solution for 20 min at RT. After several washes with PBS, cells were incubated with the primary antibodies for 1h at RT. Cells were washed several times with PBS and then incubated with the secondary antibodies for 1h at RT. Cells were washed several times with PBS and mounted on glass slides with AquaPolyMount. Stained cells were kept at 4°C before imaging. All the antibodies used during this study and their concentration are listed in Table 1. Cells were imaged using either an inverted Eclipse Ti-E microscope (NIKON) with spinning disk CSU-W1 (Yokogawa) integrated into Metamorph software (v.7.10.2.240) by Gataca Systems, a 60X water immersion lens (NA, 1.27), a 40X water immersion lens (NA, 1.15), and a 20X (NA, 0.45) objective; or an inverted laser scanning confocal Leica SP8 coupled to a multi-photon femtosecond Chameleon Vision II laser (680-1350 nm; Coherent) and a 20X water immersion lens (NA, 1.0).

Antibody	Company	Reference	Concentration	Type
Rabbit anti-Fibronectin	Sigma-Aldrich	F3648	1/400	Primary
Mouse anti-N Cadherin	Invitrogen	333900	1/400	Primary
DAPI	Thermo Scientific	D1306	1/200	
Phalloidin Rhodamine	Invitrogen	R415	1/150	
Phalloidin 633	Invitrogen	A22284	1/150	
Goat anti-Rabbit AF 647	Thermo Scientific	A32733	1/200	Secondary
Goat anti-Mouse AF 488	Invitrogen	A11029	1/200	Secondary
Donkey anti-Rabbit AF 488	Invitrogen	A21206	1/200	Secondary

Table 1. The list of antibodies used in this study.

Quantification of cell and fibronectin density

Matlab was used to do the analysis. After immunostaining and imaging of CAFs, positions were separated into topologies: comet defects, triangle defects, and aligned areas. First, the core for each position from the actin staining was pointed out and a core-centered circular mask of 400 pixels in diameter was taken. For each mask, the number of nuclei and the sum of pixel values inside the mask for fibronectin staining were calculated. Both were then normalized to the area to obtain the cell and fibronectin density. Data were pulled together into boxplots for each condition.

Nematically aligned fibronectin network preparation

To generate a nematically aligned fibronectin network, natural CAFs deposition of fibronectin was used. 5x 10^4 CAFs were seeded on 11 kPa PAA gels and cultured for 3 days in DMEM with 10% FBS, 1% ITS-A, 2% Anti-Anti, 12.5 µg/mL Metronidazole (B. Braun), and 4 µg/mL Ciprofloxacin (Panpharma) at 37°C 5% CO_2. CAFs were then removed using 1M NH_4OH for 20 min at RT. PAA gels were washed several times with PBS and the fibronectin network was stained using the immunostaining protocol without the mounting step. Finally, PAA gels were imaged to obtain a reference for fibronectin deposition. PAA gels with the fibronectin network were kept in PBS at 4°C until seeding with new CAFs.

Quantification of alignment correlation

Matlab and Fiji were used to do the analysis. The Fiji OrientationJ plugin was used for each experiment to obtain the orientation maps θ of the CAFs and fibronectin layers. For each orientation map θ, the cosinus and sinus were calculated. The cosinus matrixes of CAFs and fibronectin were then multiplied together. Similarly, the sinus matrixes of CAFs and fibronectin were also multiplied together. Both results were summed together and the absolute value of it is taken. The mean of this absolute value matrix corresponds to the average alignment correlation between the CAFs and the fibronectin layer.

Western Blot

CAFs were seeded on 30 kPa dishes (ExCellness - PrimeCoat, Biotech SA) coated with 5 µg/mL of monomeric collagen and treated with either control siRNA (siCtrl) or siRNA against fibronectin (siFN). After three days, cells were scratched and transferred to a falcon with PBS. Cells were washed twice with PBS by centrifugation for 2 min at 100 rcf. Cells were then re-suspended in 50 µL of Precellys and sonicated for 15s three times. Samples were boiled at 100°C for 10 min, then spun for 15 min at 15 900 rcf, and supernatants were diluted at one to five. Samples were then boiled at 95°C for 5 min and the same concentration of each sample was loaded into a 7,5% TGX gel and let migrate for about 1h. The proteins from the gel were transferred to a nitrocellulose membrane using Transbloc. The membrane was then incubated in 5% non-fat milk powder diluted in PBS on a shaker at RT for 1 h. The membrane was cut and then incubated at 4°C overnight with primary antibodies diluted in 1% milk/PBS solution on a shaker. The membrane was then washed three times for 5 min with PBS while shaking. The membrane was then incubated at RT for 1 h with the secondary antibodies conjugated with HRP. The membrane was then washed three times for 5 min with PBS while shaking. Cut membranes were put back together and the signal was revealed using an ECL substrate and visualized using a Chemidoc Touch Biorad.

Drugs and siRNA

All drugs used in this study are listed in Table 2. Hoechst was added just before the acquisition: CAFs were washed with PBS and then incubated with Hoechst in PBS for 30 min at 37°C, 5% CO_2. After incubation, CAFs were washed twice with PBS, cell medium was added, and acquisition was started. For siRNA treatment, CAFs were cultured for three days with siRNA on 30 kPa plates before being transferred on PAA gels. CAFs were then incubated for three more days with siRNA before launching image acquisition with siRNA present in the medium.

Drugs or siRNA	Company	Reference	Concentration	Method
AllStars Negative Control siRNA	Qiagen	1027281	100 nM	Permanently treated
Hs_FN1_6 siRNA	Qiagen	SI02664004	100 nM	Permanently treated
Hs_FN1_7 siRNA	Qiagen	SI02663997	100 nM	Permanently treated
Hoechst	Thermo Fisher	H3570	1 / 2 000	Added before acquisition

Table 2. List of the drugs and siRNA used during this study.

Quantification of defect density and size

To quantify the density of defects, four-by-four stitched image fields of view were acquired, and the comet and triangle defects were counted manually. For each type of defect, the numbers were normalized by the area. All data were then pulled together into boxplots for each condition.

The size of defects was quantified using Matlab. For each experiment, positions were separated into the types of defects: comet and triangle. For each position, defect size is taken depending on the type of defects: for the comet, size corresponded to the diameter between the head and the tail of the comet, and for the triangle, size corresponds to the distance between one vortex and the middle of the opposite side (**Fig. 2A**). All sizes were then pulled together into boxplots for each condition.

Defects trajectory analysis

The Fiji OrientationJ plugin was used for each experiment to obtain the orientation maps θ of the CAFs layers at each time point. For each experiment, positions were separated into different types of defects: comet and triangle defects. Defect cores were chosen to follow defect trajectory and found using the local nematic order parameter $\boldsymbol{Q}$. For each time point, the local nematic order parameter $\boldsymbol{Q}$ is calculated from the orientation maps θ using the following formula: $\boldsymbol{Q}=\sqrt{\langle cos2\theta\rangle^2+\langle sin2\theta\rangle^2}$. The defect core was then found from the Q map as its minimum. Once the position of the defect core at each time point was obtained, translations of the trajectory coordinates were done to have the first time point of each core at (0,0) in the (x,y) axis. Velocity and persistence were calculated from each trajectory, using the @msdanalyser of Matlab for persistence. Finally, all trajectories were plotted together for each type of topology, and boxplots for the velocities and persistence were obtained.

Cells trajectory analysis

Cells' trajectory was obtained by using Hoechst to stain nuclei or mixing a small proportion of LifeAct-GFP expressing CAFs with non-labeled CAFs and performing time-lapse imaging. For each position, Fiji was used to apply a threshold on images with the fluorescence of interest to generate binary images where each cell was well separated from the others. Thresholded images were then uploaded into Ilastik for each position to track cell trajectories. Each cell's trajectory was saved into a file. Using Matlab, translations of cell trajectory coordinates were then done to have the first-time point of each cell at (0,0) in the (x,y) axis. Velocity and persistence were extracted from each trajectory, using the @msdanalyser of Matlab for persistence. Finally, all cell trajectories were plotted together as well as boxplots for the velocities and persistence obtained.

Quantification of the evolution of the fluid flow

Using Matlab, the velocity field of the whole CAF layer was calculated using the Particle Image Velocity (PIV) method. The PIV was used on the bright field images of the whole CAF layer. The displacement in CAF position from one-time point to the next one was measured on one hundred-by-one hundred pixels squares along all images with overlapping between each square to precise the measure. From the displacement and time-laps between each image, the velocities were calculated in each square, giving rise to the velocity fields at each time point. Finally, for each time point and condition, means of the velocity fields were taken and plotted over time to show the evolution of the fluid flow.

References

1 Sahai, E. *et al.* A framework for advancing our understanding of cancer-associated fibroblasts. *Nat Rev Cancer* **20**, 174-186 (2020). https://doi.org:10.1038/s41568-019-0238-1

2 LeBleu, V. S. & Kalluri, R. A peek into cancer-associated fibroblasts: origins, functions and translational impact. *Dis Model Mech* **11** (2018). https://doi.org:10.1242/dmm.029447

3 Barbazan, J. *et al.* Cancer-associated fibroblasts actively compress cancer cells and modulate mechanotransduction. *Nat Commun* **14**, 6966 (2023). https://doi.org:10.1038/s41467-023-42382-4

4 Bhattacharjee, S. *et al.* Tumor restriction by type I collagen opposes tumor-promoting effects of cancer-associated fibroblasts. *J Clin Invest* **131** (2021). https://doi.org:10.1172/JCI146987

5 Nia, H. T. *et al.* Solid stress and elastic energy as measures of tumour mechanopathology. *Nat Biomed Eng* **1** (2016). https://doi.org:10.1038/s41551-016-0004

6 Stylianopoulos, T. *et al.* Causes, consequences, and remedies for growth-induced solid stress in murine and human tumors. *Proc Natl Acad Sci U S A* **109**, 15101-15108 (2012). https://doi.org:10.1073/pnas.1213353109

7 Attieh, Y. & Vignjevic, D. M. The hallmarks of CAFs in cancer invasion. *European Journal of Cell Biology* **95**, 493-502 (2016). https://doi.org:10.1016/j.ejcb.2016.07.004

8 Barbazan, J. & Matic Vignjevic, D. Cancer associated fibroblasts: is the force the path to the dark side? *Curr Opin Cell Biol* **56**, 71-79 (2019). https://doi.org:10.1016/j.ceb.2018.09.002

9 Pankov, R., Momchilova, A., Stefanova, N. & Yamada, K. M. Characterization of stitch adhesions: Fibronectin-containing cell-cell contacts formed by fibroblasts. *Exp Cell Res* **384**, 111616 (2019). https://doi.org:10.1016/j.yexcr.2019.111616

10 Attieh, Y. *et al.* Cancer-associated fibroblasts lead tumor invasion through integrin-beta 3-dependent fibronectin assembly. *Journal of Cell Biology* **216**, 3509-3520 (2017). https://doi.org:10.1083/jcb.201702033

11 Barbazan, J., Perez Gonzalez, C., Richon, S., Trepat, X. & D, M. V. Cancer-associated fibroblasts actively compress cancer cells and modulate mechanotransduction. . *BioRxiv* (2021). https://doi.org:2021.04.05.438443

12 Erdogan, B. *et al.* Cancer-associated fibroblasts promote directional cancer cell migration by aligning fibronectin. *J Cell Biol* **216**, 3799-3816 (2017). https://doi.org:10.1083/jcb.201704053

13 Barbier-Chebbah, A., Bénichou, O. & Voituriez, R. Self-Interacting Random Walks: Aging, Exploration, and First-Passage Times. *Physical Review X* **12**, 011052–011003 (2022).

14 d'Alessandro, J. *et al.* Cell migration guided by long-lived spatial memory. *Nat Commun* **12**, 4118 (2021). https://doi.org:10.1038/s41467-021-24249-8

15 Baschieri, F. *et al.* Fibroblasts generate topographical cues that steer cancer cell migration. *Sci Adv* **9**, eade2120 (2023). https://doi.org:10.1126/sciadv.ade2120

16 Park, D. *et al.* Extracellular matrix anisotropy is determined by TFAP2C-dependent regulation of cell collisions. *Nat Mater* **19**, 227-238 (2020). https://doi.org:10.1038/s41563-019-0504-3

17 Doostmohammadi, A., Ignes-Mullol, J., Yeomans, J. M. & Sagues, F. Active nematics. *Nat Commun* **9**, 3246 (2018). https://doi.org:10.1038/s41467-018-05666-8

18 Saw, T. B., Xi, W., Ladoux, B. & Lim, C. T. Biological Tissues as Active Nematic Liquid Crystals. *Adv Mater* **30**, e1802579 (2018). https://doi.org:10.1002/adma.201802579

19 Marchetti, M. C. *et al.* Hydrodynamics of soft active matter. *Reviews of Modern Physics* **85(3)**, 1143–1189, 1107 (2013).

20 Kawaguchi, K., Kageyama, R. & Sano, M. Topological defects control collective dynamics in neural progenitor cell cultures. *Nature* **545**, 327-331 (2017). https://doi.org:10.1038/nature22321

21 Maroudas-Sacks, Y., Garion, L., Shani-Zerbib, L., Braun, E. & Keren, K. Topological defects in the nematic order of actin fibres as organization centres of Hydra morphogenesis. *Nature Physics* **17**, 251–259 (2021). https://doi.org:10.1038/s41567-020-01083-1

22 Saw, T. B. *et al.* Topological defects in epithelia govern cell death and extrusion. *Nature* **544**, 212-216 (2017). https://doi.org:10.1038/nature21718

23 Guillamat, P., Blanch-Mercader, C., Pernollet, G., Kruse, K. & Roux, A. Integer topological defects organize stresses driving tissue morphogenesis. *Nat Mater* **21**, 588-597 (2022). https://doi.org:10.1038/s41563-022-01194-5

24 Duclos, G. *et al.* Spontaneous shear flow in confined cellular nematics. *Nat Phys* **14**, 728-732 (2018). https://doi.org:10.1038/s41567-018-0099-7

25 Duclos, G., Garcia, S., Yevick, H. G. & Silberzan, P. Perfect nematic order in confined monolayers of spindle-shaped cells. *Soft Matter* **10**, 2346-2353 (2014). https://doi.org:10.1039/c3sm52323c

26 Sarkar, T. *et al.* Crisscross multilayering of cell sheets. *PNAS Nexus* **2**, pgad034 (2023). https://doi.org:10.1093/pnasnexus/pgad034

27 Handorf, A. M., Zhou, Y., Halanski, M. A. & Li, W. J. Tissue stiffness dictates development, homeostasis, and disease progression. *Organogenesis* **11**, 1-15 (2015). https://doi.org:10.1080/15476278.2015.1019687

28 Glentis, A. *et al.* Cancer-associated fibroblasts induce metalloprotease-independent cancer cell invasion of the basement membrane. *Nature Communications* **8**, 13 (2017). https://doi.org:10.1038/s41467-017-00985-8

29 Shih, W. & Yamada, S. N-cadherin as a key regulator of collective cell migration in a 3D environment. *Cell Adh Migr* **6**, 513-517 (2012). https://doi.org:10.4161/cam.21766

30 Angheluta, L., Chen, Z., Marchetti, M. C. & Bowick, M. J. The role of fluid flow in the dynamics of active nematic defects. *New Journal of Physics* **23**, 033009 (2021).

31 Conklin, M. W. *et al.* Aligned collagen is a prognostic signature for survival in human breast carcinoma. *Am J Pathol* **178**, 1221-1232 (2011). https://doi.org:10.1016/j.ajpath.2010.11.076

32 Provenzano, P. P. *et al.* Collagen reorganization at the tumor-stromal interface facilitates local invasion. *BMC Med* **4**, 38 (2006). https://doi.org:10.1186/1741-7015-4-38

33 Trepat, X. *et al.* Physical forces during collective cell migration. *Nature Physics* **5**, 426–430 (2009).

34 Nier, V. *et al.* Inference of Internal Stress in a Cell Monolayer. *Biophys J* **110**, 1625-1635 (2016). https://doi.org:10.1016/j.bpj.2016.03.002